Biophysical Reports

ARTICLE

A common framework for single-molecule localization using sequential structured illumination

Luciano A. Masullo,[1,2] Lucía F. Lopez,[1] and Fernando D. Stefani[1,2,*]

[1]Centro de Investigaciones en Bionanociencias, Consejo Nacional de Investigaciones Científicas y Técnicas, Ciudad Autónoma de Buenos Aires, Argentina and [2]Departamento de Física, Facultad de Ciencias Exactas y Naturales, Universidad de Buenos Aires, Ciudad Autónoma de Buenos Aires, Argentina

ABSTRACT Localization of single fluorescent molecules is key for physicochemical and biophysical measurements, such as single-molecule tracking and super-resolution imaging by single-molecule localization microscopy. Over the last two decades, several methods have been developed in which the position of a single emitter is interrogated with a sequence of spatially modulated patterns of light. Among them, the recent MINFLUX technique outstands for achieving a ~10-fold improvement compared with wide-field camera-based single-molecule localization, reaching ~1–2 nm localization precision at moderate photon counts. Here, we present a common framework for this type of measurement. Using the Cramér-Rao bound as a limit for the achievable localization precision, we benchmark reported methods, including recent developments, such as MINFLUX and MINSTED, and long-established methods, such as orbital tracking. In addition, we characterize two new proposed schemes, orbital tracking and raster scanning, with a minimum of intensity. Overall, we found that approaches using an intensity minimum have a similar performance in the central region of the excitation pattern, independent of the geometry of the excitation pattern, and that they outperform methods featuring an intensity maximum.

WHY IT MATTERS Because they were developed independently and present important differences in their experimental setups and data analysis routines, various single-molecule localization methods based on sequential structured illumination, such as MINFLUX, MINSTED, or orbital tracking, have been considered as fundamentally different or slightly related. The common framework presented in this work offers conceptual order and provides insight about the essential components of all methods for single-molecule localization based on sequential structured illumination. It has practical implications too. For example, it shows that top single-molecule localization performances can be obtained on any raster-scanning microscope with minor modifications (e.g., a vortex phase plate in the excitation path).

INTRODUCTION

Since it became technically possible, localization of single fluorescent molecules has been key to obtaining information on biological processes beyond ensemble averages. For instance, single-molecule tracking measurements provide unique insight into molecular trajectories that would otherwise be hidden in the average behavior of an ensemble of unsynchronized molecules (1–5). Another important application of single-molecule localization is single-molecule localization microscopy (SMLM). In SMLM, single-molecule localization is combined with single-molecule blinking to determine the positions of a multitude of molecules in a sample. In this way, super-resolved fluorescence images can be reconstructed, in which the spatial resolution is ultimately given by the localization precision (6,7).

The performance of single-molecule tracking and SMLM is limited by the photostability of the fluorophores (7–9). Most commonly, single-molecule localization is performed using uniform illumination, and the position of the molecule is determined from a fit to its image recorded with a photodetector array such as an Electron Multiplying Charge-Coupled Device (EMCCD) or a Complementary Metal-Oxide-Semiconductor (CMOS) camera. With this approach, the lateral localization precision of organic fluorophores under biologically compatible conditions lies typically in the range of 10–50 nm. Recently, aiming to attain higher localization precisions with the available photon budget, a series of

Submitted July 6, 2021, and accepted for publication November 22, 2021.

*Correspondence: fernando.stefani@df.uba.ar

Editor: Aleksandra Radenovic.

https://doi.org/10.1016/j.bpr.2021.100036

methods have been developed in which single emitters are interrogated with a sequence of spatially modulated patterns of light. This new trend of measurements was opened by the publication of MINFLUX (10), achieving a ~10-fold improvement compared with wide-field camera-based single-molecule localization, reaching ~1–2 nm localization precision at moderate photon counts. Since then, MINFLUX has been demonstrated in model systems (DNA origami structures) and fixed and living cells, and it was recently extended to three dimensions (11,12). Also, other methods of this kind have been reported, such as Repetitive Optical Selective Exposure (ROSE) (13), SIMFLUX (14), MINSTED (15), and Modulated Localization Microscopy (MODLOC) (16). This type of single-molecule localization has been recently reviewed (17).

On the other hand, around 20 years ago, before the advent of SMLM, a method to track the motion of particles or single fluorescent molecules in two dimensions (2D) called orbital tracking (OT) was theoretically proposed (18) and later implemented experimentally in a multitude of situations, including three-dimensional (3D) tracking and combinations with fluorescence correlation spectroscopy (19–25). In OT, the fluorescence signal from a single particle or molecule is registered for a number of positions along a circular trajectory of a focused laser beam around the target molecule or particle. Other methods of single-molecule or single-particle tracking based on multiple exposures to displaced focused beams have also been reported (26–29). To the best of our knowledge, these localization techniques developed for tracking have not been combined with single-molecule blinking to obtain super-resolved images.

At first sight, because of the differences in the structure of the excitation light, instrumentation, measurement protocols, and data analysis methods, each of these methods of single-molecule localization may appear unique. Here, we show how these techniques can be regarded as special cases of a common concept of single-molecule localization using sequences of excitations with spatially structured light. We present a common analytical framework for this type of single-molecule localization and use it to 1) perform a fair benchmarking between methods and 2) identify new single-molecule localization methods that bring together the strengths of the available techniques.

MATERIALS AND METHODS

A common framework for single-molecule localization using sequential structured illumination

Fig. 1*a* shows schematically the essential components of Single-Mmolecule Localization by Sequential Structured Illumination (SML-SSI). A spatially structured excitation field $I(\boldsymbol{r})$ is sequentially shifted along a sequence of K positions $\boldsymbol{r}_i$ $(1 \leq i \leq K)$. In this study, we will deal with the 2D localization problem. Naturally, the formalism can be easily reduced to one-dimensional localization or extended to 3D localization. In 2D, the K positions $\boldsymbol{r}_i$ may be arbitrary within the plane of interest but must not be in line to avoid obvious localization ambiguities. We will call the sequence of $I(\boldsymbol{r}-\boldsymbol{r}_i)$ the "excitation pattern" and $\boldsymbol{r}_E$ the position of the emitter. For each $I(\boldsymbol{r}-\boldsymbol{r}_i)$, the emitter is exposed to a specific local intensity $I(\boldsymbol{r}_E-\boldsymbol{r}_i)$ and emits fluorescence with a certain intensity, which, in turn, corresponds to an expected value of detected photon counts (λ_i) during a given integration time. The measured fluorescence photon counts are denoted by n_i, which are assumed to be Poisson distributed with average λ_i. The latter is an excellent approximation for single photon counting detectors with neglectable dark counts such as modern avalanche photodiodes. The position of the emitter is determined from the sequence of intensity measurements $\boldsymbol{n} = [n_1,n_2,\ldots,n_K]$, and considering the known $I(\boldsymbol{r}-\boldsymbol{r}_i)$. The relationship between $I(\boldsymbol{r}_E-\boldsymbol{r}_i)$ and λ_i is assumed to be linear. This requires emission far from saturation and fluorophores rotating faster than the integration time at each position. Fluorophores with fixed orientation can be localized as well, as long as the polarization of $I(\boldsymbol{r})$ is invariant with $\boldsymbol{r}$.

Any method of single-molecule localization using sequential structured illumination can be fully described by the set of $I(\boldsymbol{r}-\boldsymbol{r}_i)$, which, in turn, is defined by the spatial structure of the excitation field $I(\boldsymbol{r})$ and the sequence of positions of the exposures $\boldsymbol{r}_i$.

We will deal with methods using focused laser beams, which can be classified into two categories depending on whether the focus has a central maximum or a central minimum (ideally a zero) of intensity. For our analysis, focused excitation fields with a central maximum will be described with a Gaussian function as

$$I_{Gauss}(\boldsymbol{r}) = A_0 e^{-4\ln 2\frac{r^2}{FWHM^2}} \quad (1)$$

and excitation fields with a central zero, here called donut-shaped foci, will be described as

$$I_{donut}(\boldsymbol{r}) = A_0 4e\ln 2\frac{r^2}{FWHM^2}e^{-4\ln 2\frac{r^2}{FWHM^2}} \quad (2)$$

Whereas for the following calculations we will use the idealized $I_{Gauss}(\boldsymbol{r})$ and $I_{donut}(\boldsymbol{r})$, we note that the analysis can be performed with any other shape of $I(\boldsymbol{r})$, particularly with functions describing more accurately experimentally determined illumination patterns. Here, we will treat $I(\boldsymbol{r})$ as a known function. In experiments, however, the best performance is obtained using a precise description of the experimental $I(\boldsymbol{r})$. For this reason, SML-SSI methods usually involve two measurements: 1) A detailed characterization of the excitation light field $I(\boldsymbol{r})$ using bright emitters (i.e., fluorescent nanoparticles) delivering almost unlimited photon counts (i.e., $N > 10^6$) and high Signal to Noise Ratio (SNR), and 2) the measurement with limited photon counts (i.e., $N < 10^3$) and low SNR by sequentially exciting the single emitter (i.e., organic fluorophore or fluorescent protein), whose position is unknown.

As for the sequence of excitation positions $\boldsymbol{r}_i$, we will also consider two types: orbital sequences enclosing an area (as it is done in OT), and raster-scanning sequences covering an area (as it is done in raster-scanning microscopy). Varying combinations of I_{Gauss}, I_{donut}, and sequences of $\boldsymbol{r}_i$ can be used to define any SML-SSI method using focused beams, including all methods reported so far and possibly many new conceptions. For example, Fig. 1*b* shows schematically the combination used for classical OT (18,19,30), namely, I_{Gauss} excitation sequentially shifted over K positions along a circle. In practice, optimum performance in OT is achieved with a radius of the circle close to half the full width at half-maximum ($FWHM$) of I_{Gauss} (19,30,31). The number of exposures K may vary from a few up to

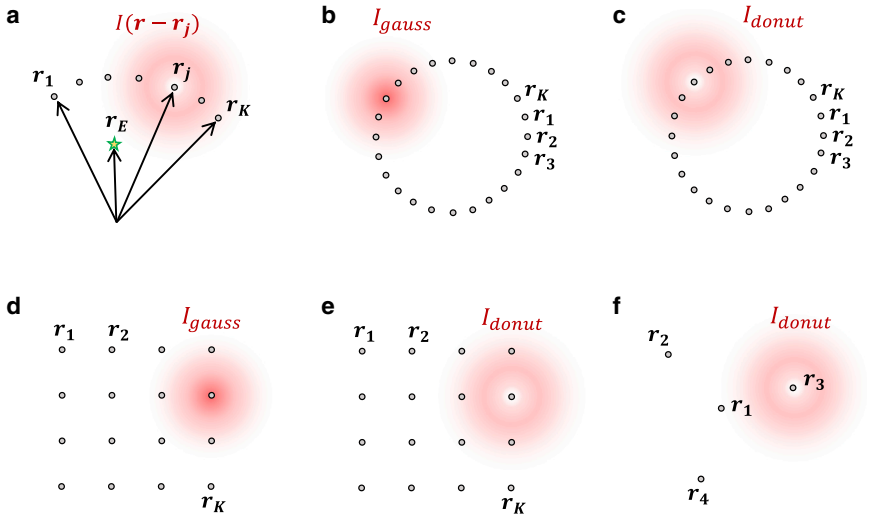

FIGURE 1 (*a*) Schematic showing the essential parameters of a SML-SSI measurement in 2D. $\boldsymbol{r}$ defines the position in the plane of interest. $I(\boldsymbol{r}-\boldsymbol{r}_i)$ is the structured excitation field located at position $\boldsymbol{r}_i$. The excitation field is sequentially placed at K positions $\boldsymbol{r}_i$ ($1 \le i \le K$). At each position of the excitation field, the intensity of an emitter placed at $\boldsymbol{r}_E$ is registered. (*b*–*f*) Example configurations of SML-SSI measurements using a maximum ($I_{G_{auss}}$) or a minimum (I_{donut}) of light.

a quasicontinuum intensity register. The so-called single-molecule confocal laser tracking (32) can be regarded as a special case of OT with $K = 6$. MINSTED (15) is, in essence, another expression of OT that achieves higher localization precision by using an effectively smaller excitation field produced by the combination of a normal excitation beam and a donut-shaped depletion beam, just as in STimulated Emission Depletion (STED) microscopy (33,34). Hence, the excitation field of MINSTED can be described by $I_{Gauss}(\boldsymbol{r})$ with an *FWHM* below the diffraction limit. Alternatively, OT could be performed with $I_{donut}(\boldsymbol{r})$, as schematically shown in Fig. 1*c*. We will call this method orbital tracking with a minimum (OTMIN). To the best of our knowledge, OTMIN has not been proposed or implemented.

The sequence of $\boldsymbol{r}_i$, can also be organized in a raster to cover an area, as shown in Fig. 1*d* for $I_{Gauss}(\boldsymbol{r})$. This configuration, here denoted as RASTMAX, has been used for single-molecule localization in trapping experiments (35) and also for super-resolved imaging in a confocal microscope (36). Under this framework, a new method, where $I_{donut}(\boldsymbol{r})$ is raster scanned over a rectangular area, can be easily envisaged, as schematically shown in Fig. 1*e*; we will call this new scheme raster scanning with an intensity minimum (RASTMIN). Finally, Fig. 1*f* shows the scheme of 2D MINFLUX, where $I_{donut}(\boldsymbol{r})$ is shifted over four positions, a central exposure and three more forming an equilateral triangle around the central position (10,37). 2D MINFLUX can be classified as a raster-scanning method because the excitation pattern used is the minimum needed to cover an area.

Position estimation and precision

Estimating the molecular position from the intensity measurements $\boldsymbol{n} = [n_1, n_2, \ldots, n_K]$ and $I(\boldsymbol{r}-\boldsymbol{r}_i)$ can be done in innumerable ways, and many have been implemented in the various methods cited above. For example, in OT, the position of the emitter has been estimated by analyzing quasicontinuum intensity signals by Fourier analysis (19) or by triangulation of discrete intensity signals (32). In MINFLUX (10,37) or the four-focus single-particle localization (26), the position of the emitter is obtained using a maximum likelihood estimator (MLE) with four intensity measurements. Other methods, such as MINSTED (15), use other ad hoc analysis functions and routines.

Ideally, the position estimator must be unbiased and precise. Using the Fisher information matrix, a theoretical maximum precision for an unbiased position estimator can be calculated in the form of a theoretical lower bound for the variance of the estimator, the so-called Cramér-Rao bound (*CRB*) (38). Here, we will use the MLE to determine the emitter position from $\boldsymbol{n}$ and $I(\boldsymbol{r}-\boldsymbol{r}_i)$. The MLE is by far the most widely used approach in statistical estimation because of its well-established performance; it is, in general, consistent and asymptotically attains the *CRB* (38). The MLE has been successfully used for single-molecule localization in camera-based approaches (39–41) as well as in sequential structured illumination approaches, such as in the 3D four-focus localization (26) or MINFLUX (10). Following the same procedure to estimate the emitter position as in these previous works, the likelihood function L for the emitter position can be expressed as

$$\mathcal{L}(\boldsymbol{r}_E|\boldsymbol{n}) = \frac{N!}{\prod_{i=1}^{K} n_i!} \prod_{i=1}^{K} p_i(\boldsymbol{r}_E)^{n_i} \tag{3}$$

where $N = \sum_{i=1}^{K} n_i$ is the total number of detected photons, and $p_i(\boldsymbol{r}_E)$ is the multinomial parameter for each exposure

$$p_i(\boldsymbol{r}_E) = \frac{I(\boldsymbol{r}_E - \boldsymbol{r}_i)}{\sum_{j=1}^{K} I(\boldsymbol{r}_E - \boldsymbol{r}_j)} \tag{4}$$

defined as the ratio between the intensity of the excitation field at the fluorophore position for the current exposure and the sum of all the exposure intensities. In the presence of background, defined by the Signal-to-Background Ratio (*SBR*), Eq. 4 becomes

$$p_i(\boldsymbol{r}_E) = \frac{SBR(\boldsymbol{r}_E)}{SBR(\boldsymbol{r}_E)+1} \frac{I(\boldsymbol{r}_E - \boldsymbol{r}_i)}{\sum_{j=1}^{K} I(\boldsymbol{r}_E - \boldsymbol{r}_j)} + \frac{1}{SBR(\boldsymbol{r}_E)+1} \frac{1}{K} \tag{5}$$

A detailed derivation of Eq. 5 is described in Supporting materials and methods, Section 1. It is based on three assumptions about the background contribution: 1) it does not depend on the position of the emitter, 2) it is Poisson distributed, and 3) it is equal for all exposures. The first assumption holds in any experiment. The second one implies that we considered background any detectable photons reaching the detector that do not originate from the target molecule. In experiments, the background contribution would come mainly from fluorescence of the coverslip or other sample components (including any out-of-focus contribution), but it could also include, for example, scattered light from other light sources of the

lab, as well as scattered and/or reflected light of the excitation lasers that is not fully blocked by the optical filters. Dark counts of the detectors could also be taken into account with Eq. 5 as long as they are Poisson distributed. This is a good approximation for measurements with single-photon counting detectors, such as avalanche photodiodes, as confirmed experimentally (10,37). We also note that with this type of detectors, because there is no readout noise, the background level does not depend on the number of exposures K but only on the integration time. Other, non-Poissonian, detector noise as found, for example, in photomultiplier tubes or EM-CCD cameras, is not considered in Eq. 5.

The third assumption is satisfied if the detection volume is large enough to detect the complete background excited by $I(\boldsymbol{r} - \boldsymbol{r}_i)$ for all the $\boldsymbol{r}_i$ positions. We remark that SML-SSI methods do not impose any requirement on the detection volume. All the information is retrieved from the structured sequential excitation. Nonetheless, applying restrictions to the detection volume, for example using confocal detection, could be advantageous to reduce background contributions. In such cases, overall higher *SBR* levels would be obtained, but the background contribution generated by each exposure $I(\boldsymbol{r} - \boldsymbol{r}_i)$ would be different and dependent on the particular $I(\boldsymbol{r})$, the exposure position $\boldsymbol{r}_i$, and the geometry and relative position of the detection volume. For example, for a strict confocal detection concentric with the excitation pattern and a large excitation pattern of size comparable to the diffraction limit, the background contributions of the central exposures would be larger than the exposures at the periphery. By contrast, in the case of a relaxed confocal detection volume (e.g., twofold the diffraction limit) and subdiffraction excitation patterns, the background contributions of all exposures are expected to be practically identical. To keep the general applicability of the formalism and to stress that a confined detection volume is not a requisite for SML-SSI, we considered the background contributions of all exposures equivalent.

$SBR(\boldsymbol{r}_E)$ can be obtained from an assumption or experimental determination of *SBR* at the center of the excitation pattern $SBR(\boldsymbol{0})$, as

$$SBR(\boldsymbol{r}_E) \;=\; SBR(0)\,\frac{\sum_{j=1}^{K} I\left(\boldsymbol{r}_E - \boldsymbol{r}_j\right)}{\sum_{j=1}^{K} I\left(0 - \boldsymbol{r}_j\right)}\,. \tag{6}$$

In the following, we will use $SBR(\boldsymbol{0}) \equiv SBR$ as a scalar parameter for the benchmarking of the different methods.

For the MLE, it is practical to use the log-likelihood function $l(\boldsymbol{r}_E|\boldsymbol{n}) = \ln(\mathcal{L}(\boldsymbol{r}_E|\boldsymbol{n}))$:

$$l(\boldsymbol{r}_E|\boldsymbol{n}) \;=\; \sum_{i=0}^{K} \ln(p_i(\boldsymbol{r}_E)\,)n_i \tag{7}$$

because we are interested in finding the value of $\boldsymbol{r}_E$ that maximizes the function. In Eq. 7, all additive constants have been omitted because they are irrelevant for the maximum likelihood estimation of the emitter position, which is computed as follows:

$$\widehat{\boldsymbol{r}_E}^{MLE} \;=\; \operatorname{argmax}\,(l(\boldsymbol{r}_E|\boldsymbol{n})) \tag{8}$$

In general, SML-SSI delivers high-precision position estimations only for molecules in the vicinity of the excitation pattern. Furthermore, molecules too far from the excitation pattern remain undetectable. Thus, in real-life experiments, lower-precision information about the emitter position is necessary to place the excitation pattern in the vicinity of the target molecule. The likelihood function can be modified to include this prior as follows:

$$\mathcal{L}(\boldsymbol{r}_E|\boldsymbol{n}) \;=\; \frac{N!}{\prod_{i=1}^{K} n_i!} \prod_{i=1}^{K} p_i(\boldsymbol{r}_E)^{n_i} f(\boldsymbol{r}_E) \tag{9}$$

where the function $f(\boldsymbol{r}_E)$ includes the prior information about the emitter position. The log-likelihood function then becomes

$$l\left(\boldsymbol{r}_E|\boldsymbol{n}\right) \;=\; \sum_{i=1}^{K} n_i \ln p_i(\boldsymbol{r}_E|\boldsymbol{n}\Big) + \ln f(\boldsymbol{r}_E) \tag{10}$$

where, again, all the constant terms have been dropped because we are only interested in the maximum of the $l(\boldsymbol{r}_E|\boldsymbol{n})$ function. We note that f may depend on an independent set of photon counts used to determine the molecule position with low precision.

For the 2D problem, $\boldsymbol{r}_E = (x,y)$ and the Fisher information matrix takes the form

$$\mathcal{J}(\boldsymbol{r}_E) \;=\; -E\left(\begin{bmatrix} \dfrac{\partial^2 l(\boldsymbol{r}_E|\boldsymbol{n})}{\partial x^2} & \dfrac{\partial^2 l(\boldsymbol{r}_E|\boldsymbol{n})}{\partial x \partial y} \\ \dfrac{\partial^2 l(\boldsymbol{r}_E|\boldsymbol{n})}{\partial y \partial x} & \dfrac{\partial^2 l(\boldsymbol{r}_E|\boldsymbol{n})}{\partial y^2} \end{bmatrix}\right) \tag{11}$$

which, using Eq. 10 can be expressed as

$$\mathcal{J}(\boldsymbol{r}_E) \;=\; \mathcal{J}_{SML-SSI} + \mathcal{J}_{prior} \;=$$

$$N \sum_{i=1}^{K} \frac{1}{p_i} \begin{bmatrix} \left(\dfrac{\partial p_i}{\partial x}\right)^2 & \dfrac{\partial p_i}{\partial x}\dfrac{\partial p_i}{\partial y} \\ \dfrac{\partial p_i}{\partial y}\dfrac{\partial p_i}{\partial x} & \left(\dfrac{\partial p_i}{\partial y}\right)^2 \end{bmatrix} - \begin{bmatrix} \dfrac{\partial^2 \ln f}{\partial x^2} & \dfrac{\partial^2 \ln f}{\partial x \partial y} \\ \dfrac{\partial^2 \ln f}{\partial y \partial x} & \dfrac{\partial^2 \ln f}{\partial y^2} \end{bmatrix} \tag{12}$$

Finally, the lower bound for the covariance matrix of the estimated emitter position as a function of the real emitter position $\Sigma_{cov}(\boldsymbol{r}_E)$ can be obtained from the van Trees inequality, also known as Bayesian *CRB* (42,43)

$$\Sigma_{cov}(\boldsymbol{r}_E) \geq \Sigma_{CRB}(\boldsymbol{r}_E) \;=\; \mathcal{J}(\boldsymbol{r}_E)^{-1} \tag{13}$$

For simplicity, we will take the arithmetic mean of the eigenvalues of $I(\boldsymbol{r}_E)^{-1}$ as a measure of the average maximal precision

$$\sigma_{CRB}(\boldsymbol{r}_E) \;=\; \sqrt{\frac{1}{D} tr\,[\Sigma_{CRB}(\boldsymbol{r}_E)\,]} \tag{14}$$

where D is the number of dimensions of the localization problem; in this work $D = 2$. In general, $f(\boldsymbol{r}_E)$ reduces the uncertainty in the position estimation. To visualize this, it can be considered that any prior can be expressed, at least approximately, as a Gaussian function or similar centered at the estimated position, whose logarithm has a second derivative that is always negative.

The implementation of this mathematical formalism was written in Python and is fully open-source. All functions and scripts used in this work can be found in the following repositories https://github.com/lumasullo/sml-ssi and https://github.com/stefani-lab/sml-ssi, where instructions are also provided to reproduce all calculations of this study as well as to vary parameters for other calculations.

RESULTS AND DISCUSSION

Benchmarking different methods

Next, we benchmark the theoretical performance of different orbital and raster-scanning SML-SSI methods, including reported techniques and new proposals. The size of the excitation pattern is a relevant parameter for all methods. We parametrize it by L, the diameter of the orbit or the diagonal of the raster, for orbital or scanning methods, respectively. For each method we show an exemplary 2D map of σ_{CRB} for a set of realistic experimental parameters ($N = 500$ detected photons, $SBR = 5$) and the average σ_{CRB} ($\overline{\sigma}_{CRB}$) within a circular field-of-view (*FOV*) concentric with the excitation pattern and size ranging from 10 to 300 nm. Also, for an *FOV* with a diameter of 0.75L, which is a suitable localization region for all methods, we evaluate the average localization precision $\overline{\sigma}_{CRB}$ as a function of N and *SBR*. In all cases, we used a Gaussian prior $f(\boldsymbol{r}_E)$ that represents a rough previous localization of the emitter ($\sigma_{prior} = 50$ nm (i.e., *FWHM* ∼118 nm)), which is a common step of all real-life experiments of this kind. The cost in photon budget of this prior information is not analyzed because it would be the same for all the methods; it would lay in the $N = 50$–100 range, depending on the procedure used.

Orbital methods

We first analyze orbital methods using I_{Gauss} excitation. We note that, theoretically, the localization precision using Gaussian beams increases indefinitely with L. However, in practice, the drop in *SBR* leads to a compromise value of the orbit roughly equal to the *FWHM* (19,31). Therefore, all orbital methods using a Gaussian beam will be studied for $L = FWHM$.

Fig. 2*a* shows a map of the localization precision (σ_{CRB}) for OT with $L = FWHM = 300$ nm, $K = 100$, $N = 500$, and $SBR = 5$. The performance is approximately flat in areas up to $\sim L^2$. This behavior is also evident in the curves of $\overline{\sigma}_{CRB}$ versus size of the *FOV* for OT ($L = 300$ nm) and MINSTED ($L = 100$ nm and $L = 50$ nm) in Fig. 2*b* . For the case of $L = 50$ nm, it can be observed that the localization uncertainty increases up to 20–30 nm for $FOV > 5L$. A similar behavior is observed for all OT implementations scaled by L. Also in Fig. 2*b* , the performance of these methods is shown for $K = 6$ (*dotted lines*). Particularly, the diffraction-limited case ($L = 300$ nm) with $K = 6$ corresponds to the method recently reported as single-molecule confocal laser tracking (32). The theoretical localization precision achieved with just six exposures is practically the same as with its quasicontinuous counterpart ($K = 100$).

Fig. 2*c* and *d* show the $\overline{\sigma}_{CRB}$ over an *FOV* with a diameter of 0.75L as a function of *SBR* and N, respectively. Both continuous (*solid line*) and discrete (*stars*) versions show almost identical behaviors and are strongly influenced by the size of $FWHM = L$, which explains the better precision achieved with MINSTED. Attaining 1-nm precision with $N = 1000$–3000 is only possible with $L <$ 100 nm (i.e., by means of STED or any other way to achieve subdiffraction effective excitation fields).

Next, we analyze the performance of a method featuring a minimum of intensity in the excitation

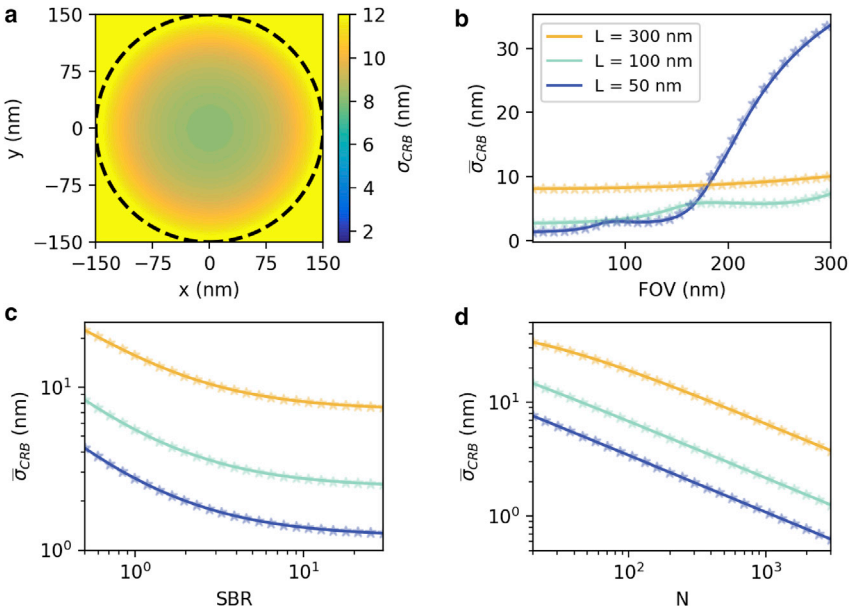

FIGURE 2 Orbital tracking, single-molecule confocal tracking, and MINSTED. (*a*) Precision map $\sigma_{CRB}(x,y)$ for $L = FWHM = 300$ nm, $K = 100$. The black dotted line indicates the orbit. (*b*) $\overline{\sigma}_{CRB}$ as a function of the *FOV* size for $K = 100$ (*solid*) and $K = 6$ (*stars*) for three values of $L = FWHM$. (*c*) $\overline{\sigma}_{CRB}$ for a $FOV = 0.75\,L$ as a function of *SBR*. (*d*) $\overline{\sigma}_{CRB}$ for a $FOV = 0.75\,L$ as a function of N. Parameters: $N = 500$, $SBR = 5$, unless otherwise stated.

beam (I_{donut}) and an orbital sequence of exposures. To our knowledge, such a method has not been realized experimentally. We will refer to it as OTMIN.

Fig. 3*a* shows a 2D map of σ_{CRB} for OTMIN with $L = 100$ nm and $K = 100$. In contrast to OT, OTMIN can be performed with orbits of arbitrarily small size without the need of applying subdiffraction techniques. OTMIN delivers accurate localizations in the inner part of the orbit. Remarkably, in the region close to the orbit, the σ_{CRB} increases rapidly. Monte Carlo simulations confirm that the OTMIN estimator is accurate and reaches the *CRB* in the inner part of the area defined by the orbit (Fig. S1*a*) but becomes imprecise and inaccurate in the vicinity of the orbit (Fig. S1*b*). Nonetheless, this ill-behaved region is very narrow. Experimentally, it could be avoided by injecting information to the measurement to use an *FOV* limited to the well-behaved area (e.g., periodically recentering the pattern in real time).

Fig. 3*b* shows curves of $\overline{\sigma}_{CRB}$ versus size of the *FOV* for OTMIN with $L = 50$, 100, and 150 nm for $K = 100$ (*solid*) and $K = 6$ (*stars*). The performance of OTMIN is practically identical for $K = 100$ and $K = 6$. The best achievable localization precision of OTMIN improves with decreasing values of L (for a constant $FWHM = 300$ nm of the focused beam). This increase in localization precision at the expense of limiting the *FOV* is a common feature of all methods using a minimum of intensity. Experimentally, the ultimate limit to shrink L is the decrease in *SBR*. Whereas the *FOV* can have a subdiffraction size, the illumination and detection volumes are still diffraction-limited. Thus, for a given illumination intensity, reducing L to subdiffraction dimensions reduces the excitation and fluorescence emission of the emitters, but the background contribution remains constant.

In all cases, for an *FOV* size of up to $0.75L$, the average localization precision of OTMIN remains remarkably high. For example, for $N = 500$ and $SBR = 5$, OTMIN reaches an average precision of, $\overline{\sigma}_{CRB} < 2$ nm,with $L = 100$ nm, or $\overline{\sigma}_{CRB} < 1$ nm, with $L = 50$ nm (Fig. 3*c-d*). This level of performance is only comparable to the best reported localization precision attained with MINFLUX. Remarkably, a recent publication reports a development of MINFLUX for which six orbital exposures are used and a central exposure is presented as optional (12), which is effectively the configuration shown here for OTMIN with $K = 6$. We note that this result could be of particular interest for several labs in the world that already have OT setups. Their localization precision could be increased significantly simply by adding a suitable phase mask in the excitation path to generate a focus with a central minimum.

Raster methods

MINFLUX, using just four exposures ($K = 4$) with the excitation pattern I_{donut}, can be regarded as the minimal expression of a raster method. Three of the exposures delimit an area that is probed with just one central exposure. MINFLUX performance has been comprehensively studied, both theoretically and experimentally (10,11). Here, we reproduce (for completeness) and expand the reported theoretical results. We note, however, that our calculations include the spatial dependency of $SBR(x,y)$ instead of using the approximation

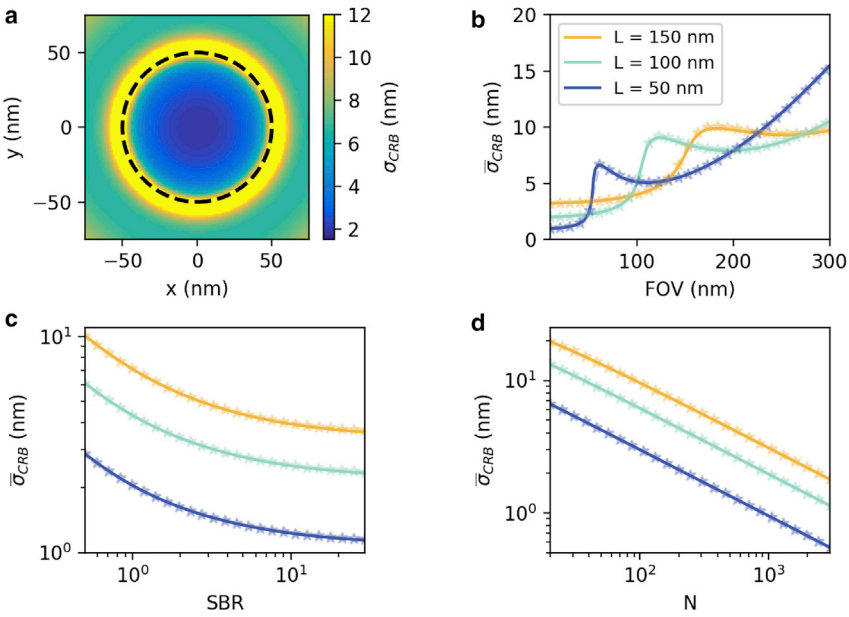

FIGURE 3 OTMIN. (*a*) Precision map $\sigma_{CRB}(x,y)$ for $L = 100$ nm. The black dotted line indicates the orbit. (*b*) $\overline{\sigma}_{CRB}$ as a function of the *FOV* size. (*c*) $\overline{\sigma}_{CRB}$ for a $FOV = 0.75\ L$ as a function of *SBR*. (*d*) $\overline{\sigma}_{CRB}$ for a $FOV = 0.75\ L$ as a function of *N*. Parameters: $K = 100$ (*solid*) and $K = 6$ (*stars*), $FWHM = 300$ nm, $N = 500$, $SBR = 5$, unless otherwise stated.

of a constant $SBR(x,y) = SBR(0,0)$. Fig. 4*a* shows a map of σ_{CRB} for MINFLUX with $L = 100$ nm, $N = 500$, $SBR = 5$, and $FWHM = 300$ nm. Fig. 4*b* displays curves of $\overline{\sigma}_{CRB}$ versus size of the *FOV* for $L = 50$, 100, and 150 nm ($N = 500$ and $SBR = 5$); the central exposure of MINFLUX directly solves the problems of OTMIN close to the orbit border, and no local maximum in uncertainty appears for $FOV \sim L$. As already reported, MINFLUX delivers the best localization precision at the center of the excitation pattern, a common feature of all these methods. For instance, with $N = 500$, $SBR = 5$, and $L = 100$ nm, the average precision is $\overline{\sigma}_{CRB} = 2.7$ nm for an $FOV = 0.75\,L$, whereas the precision at the center of the excitation pattern is σ_{CRB} (0,0) = 2.0 nm. The localization precision of MINFLUX is the best demonstrated to date, achieving $\overline{\sigma}_{CRB} < 1$ nm for $L = 50$ nm and $N \geq 800$ and $SBR \geq 5$ (Fig. 4*d*). It should be noted that as *L* is decreased, the precision at the center of the excitation pattern increases, but $\overline{\sigma}_{CRB}(FOV)$ grows more rapidly (Fig. 4*b*), especially outside the region defined by the excitation pattern. For example, $\overline{\sigma}_{CRB}$ ($FOV = 200$ nm) ~6 nm for $L = 100$ nm, whereas $\overline{\sigma}_{CRB}$ ($FOV = 200$ nm) ~10 nm for $L = 50$.

Another method of this kind consists of using exposures of a minimum of intensity organized in a rectangular raster. To our knowledge, such a method has not been reported either theoretically or experimentally. We will refer to it as raster scanning with a minimum (RASTMIN). Fig. 5*a* shows a 2D map of $\sigma_{CRB}(x,y)$ for RASTMIN with $L = 100$ nm, $N = 500$, and $SBR = 5$. As it happens with MINFLUX, the central exposures in RASTMIN solve the ill-behaved area that appears in OTMIN for $FOV \sim L$ (Fig. 5*b*).

The performance of RASTMIN in terms of *SBR* (Fig. 5*c*) and *N* (Fig. 5d) is very similar to MINFLUX and OTMIN. For $SBR > 5$, it reaches precisions of ~1 nm for $N = 500$ and $N = 1000$ for $L = 50$ and $L = 100$ nm, respectively (Fig. 5*d*).

In principle, RASTMIN can be performed in any laser scanning (confocal) microscope because they are readily prepared to perform rectangular raster scans. The only hardware modification needed would be including a phase mask into the excitation beam path to produce a focus featuring a central minimum (ideally a zero) of intensity. In this way, the power of localizing with intensity minima could be made available to significantly more optical systems available in many labs. We note, however, that achieving nanometer localization precision requires active stabilization or drift correction systems with nanometer accuracy (46).

We also analyze the performance of the counterpart of RASTMIN using excitation maxima. For the purpose of comparison to the other methods, we will denote this approach RASTMAX. For a sufficiently large *L* this approach is equivalent to conventional laser scanning (confocal) imaging and localization of the single emitter that has been reported first in the context of tracking (35) and more recently for super-resolution imaging (36).

Fig. 6*a* shows a map of σ_{CRB} for RASTMAX with $FWHM = 300$ nm, $L = 600$ nm, $N = 500$ and $SBR = 5$. Within the region of interest defined by $FOV = 0.75L$, the average localization precision ranges from 7 to 9 nm. Contrary to what happens in RASTMIN, excitation patterns smaller than the *FWHM* of the excitation beam decrease the precision achieved by RASTMAX (Fig. 6b ,

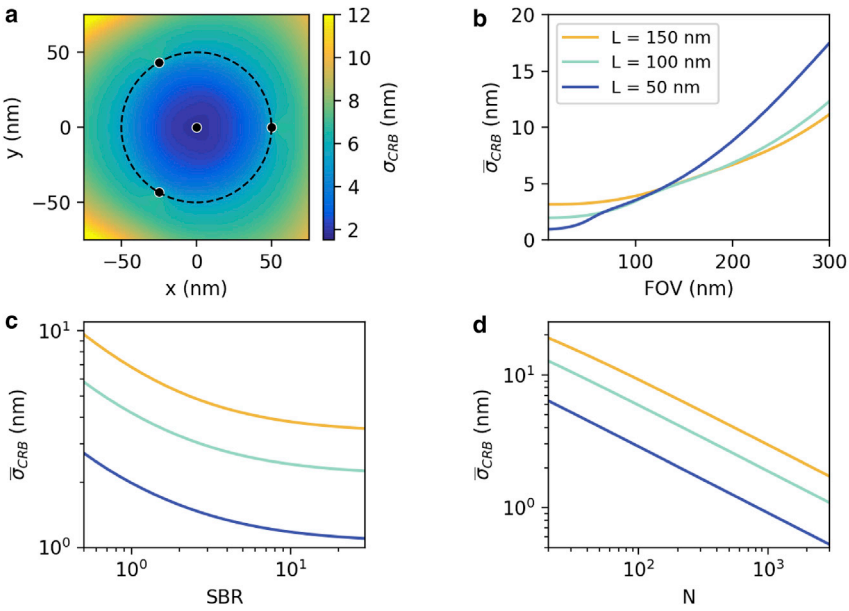

FIGURE 4 MINFLUX. (*a*) Precision map $\sigma_{CRB}(x,y)$ for $L = 100$ nm. Black dotted line indicates a circle of diameter *L*, black dots indicate the positions $\boldsymbol{r}_i$ of the exposures. (*b*) $\overline{\sigma}_{CRB}$ as a function of the *FOV*. (*c*) $\overline{\sigma}_{CRB}$ for a $FOV = 0.75\,L$ as a function of *SBR*. (*d*) $\overline{\sigma}_{CRB}$ for a $FOV = 0.75\,L$ as a function of *N*. Parameters: $K = 100$, $FWHM = 300$ nm, $N = 500$, $SBR = 5$, unless otherwise stated.

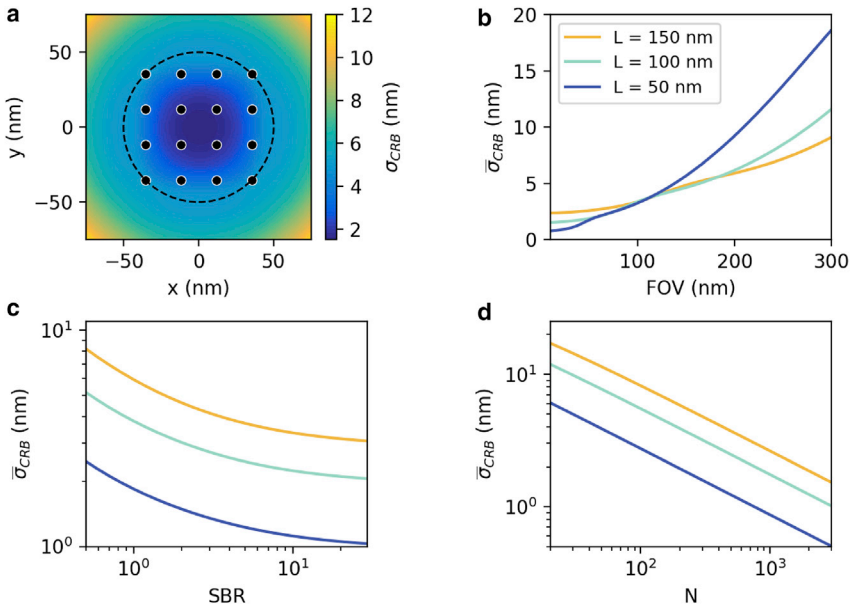

FIGURE 5 Raster scanning with a minimum. (*a*) Precision map $\sigma_{CRB}(x,y)$ for $L = 100$ nm. Black dotted line indicates a circle of diameter L; black dots indicate the positions $\boldsymbol{r}_i$ of the exposures. (*b*) $\overline{\sigma}_{CRB}$ as a function of the *FOV*. (*c*) $\overline{\sigma}_{CRB}$ for a $FOV = 0.75\,L$ as a function of *SBR*. (*d*) $\overline{\sigma}_{CRB}$ for a $FOV = 0.75\,L$ as a function of N. Parameters: $K = 16$, $FWHM = 300$ nm, $N = 500$, $SBR = 5$, unless otherwise stated.

solid lines). Given a certain *FWHM*, we find that $L < FWHM$ gives poor results in terms of precision because the part of the excitation beam with more sensitivity, the flanks of the Gaussian focus, are not used to excite the emitter. On the other hand, using $L >> FWHM$ is not optimal either because most exposures would not excite the emitter efficiently and only contribute to add background to the measurement. Hence, an optimal situation is given by $L \sim 2\ FWHM$.

It is of interest to analyze RASTMAX with subdiffraction excitation maxima attained, for example, through STED. To our knowledge, such a nanoscopy scheme has not yet been realized, although experimental results of STED nanoscopy on immobilized single molecules have been reported (44,45). We study the potential performance of such a method by considering a RASTMAX scheme with $FWHM = 50$ nm and $L = 100$ nm. As can be seen in Fig. 6*b* (*blue*, *dotted line*), such a method has the potential to reach precisions comparable to MINSTED.

RASTMAX precision as a function of *FOV* remains fairly constant up to $FOV = 2L$, where it starts to decrease, mainly because of a drop in relative *SBR* (Fig. 6*b*). On the other hand, the precision as a function of *SBR* decays similarly to the other methods (Fig. 6*c*). The calculations indicate that ∼4-nm precision should be reached for $N \sim 1000$ with an $SBR = 5$ (Fig. 6*d*). Although it does not match the precisions of MINFLUX, OTMIN, or RASTMIN, RASTMAX should significantly outperform camera-based SMLM. The reason for this is that the measurement process in a single-photon counting detector, such as avalanche photodiodes is well described by Poisson noise, whereas detecting with a camera involves other sources of noise that compromise localization precision at relatively low photon numbers (9). A comparison between RASTMAX and a hypothetical camera detection with purely Poisson noise is described in Supporting materials and methods, Section 2.

Top performance comparison

Finally, we made a comparison of reported and new methods under optimum conditions for each one. Fig. 7 summarizes these results. The already known methods (OT, MINSTED, MINFLUX, RASTMAX) were evaluated using the best combinations of parameters that have been experimentally realized. For the new methods (OTMIN, RASTMIN), we chose optimum parameters that are experimentally realizable. An $FWHM = 300$ nm was used for all diffraction-limited foci. When a subdiffraction maximum of intensity was used (MINSTED) we considered an $FWHM = 50$ nm. Each method was evaluated for the best-performing and realistic value of L: $L_{OT} = 300$ nm, $L_{RASTMAX} = 600$ nm, and $L_{MINSTED} = L_{MINFLUX} = L_{RASTMIN} = L_{OTMIN} = 50$ nm. In all cases, $SBR = 5$, and a total photon count $N = 500$ were considered.

Among the methods that use diffraction-limited excitation, the ones using a minimum of intensity achieve a ∼5-fold better precision than the ones using a maximum, regardless of the sequence of exposures (Fig. 7*a*). Methods using subdiffraction excitation maxima (i.e., MINSTED) can achieve a precision up to ∼1 nm by engineering an effective point spread function well below the diffraction limit of light.

In general, all techniques present the best performance in the central region of the excitation pattern over an area ∼75–80% of the range defined by the L (Fig. 7*b*). In this

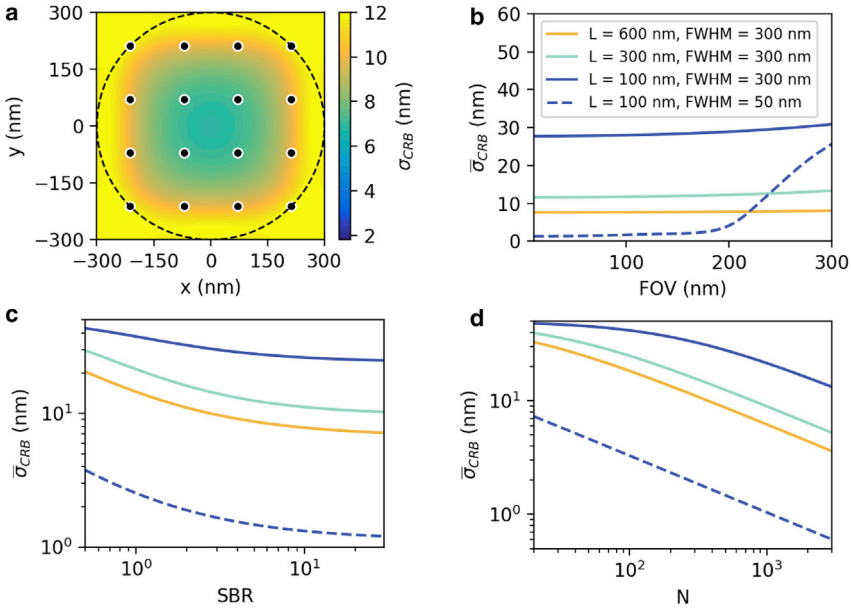

FIGURE 6 Raster scanning with a maximum. (*a*) Precision map $\sigma_{CRB}(x,y)$ for $L = 600$ nm. Black dotted line indicates a circle of diameter L; black dots indicate the positions $\boldsymbol{r}_i$ of the exposures. (*b*) $\overline{\sigma}_{CRB}$ as a function of the *FOV*. (*c*) $\overline{\sigma}_{CRB}$ for a $FOV = 0.75\,L$ as a function of *SBR*. (*d*) $\overline{\sigma}_{CRB}$ for a $FOV = 0.75\,L$ as a function of N. Parameters: $K = 16$, $N = 500$, $SBR = 5$, unless otherwise stated. *FWHM* = 300 nm (*solid lines*), *FWHM* = 50 nm (*dotted line*).

regard, methods featuring maxima are more robust and perform well over larger regions of space.

For $SBR > 5$, the localization precision of all techniques is always better than 75% of the ideal precision for infinite *SBR* (Fig. 7*c*). Detailed numbers on the analysis of precision with respect to *SBR* and *FOV* are given in Table S1. Methods using a minimum of intensity are ∼10–20 times more photon efficient, reaching molecular scale precision (σ_{CRB} ∼1 nm) with N ∼1000. Methods using a maximum of intensity are limited to σ_{CRB} ∼3–5 nm for $N = 1000$–3000 and require much higher photon budgets ($N \geq 30{,}000$) to achieve σ_{CRB} ∼1 nm.

CONCLUSIONS

We have presented a framework that is common to all SML-SSI, such as OT or MINFLUX. Under this framework, using a formalism based on information theory and maximum likelihood estimation, we made a fair comparison between methods by means of the Cramér-Rao bound of the localization precision, which is independent of the estimator used to infer the position of the emitter. Only the Poisson shot noise of the photon counts was considered. In this way, we computed the maximal possible localization precision,

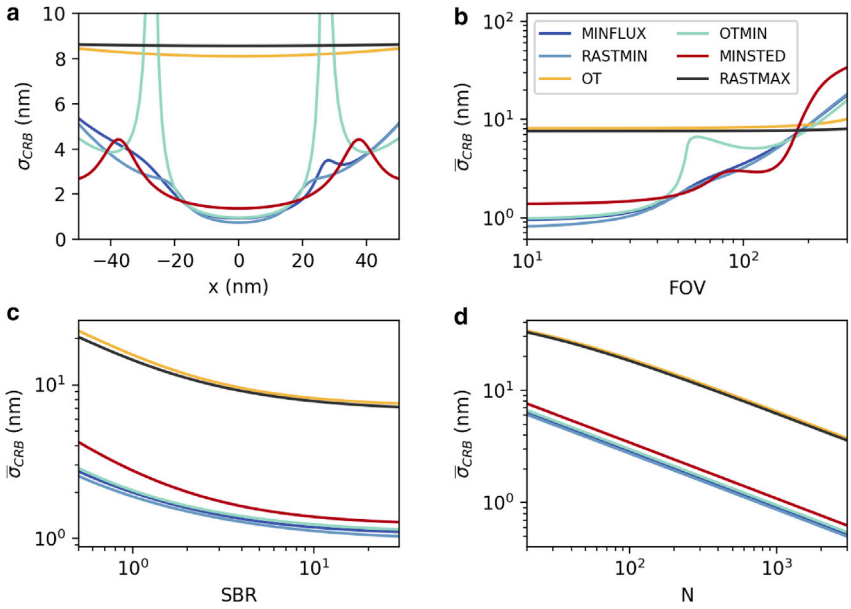

FIGURE 7 Comparison of the different methods. (*a*) One-dimensional profile ($y = 0$) of the precision map $\sigma_{CRB}(x,y)$ for all the methods using their best-performing realistic parameters. An *FWHM* = 300 nm was used for all diffraction-limited foci. For MINSTED, we considered an *FWHM* = 50 nm. L: $L_{OT} = 300$ nm, $L_{RASTMAX} = 600$ nm, and $L_{MINSTED} = L_{MINFLUX} = L_{RASTMIN} = L_{OTMIN} = 50$ nm. (*b*) $\overline{\sigma}_{CRB}$ as a function of the *FOV*. (*c*) $\overline{\sigma}_{CRB}$ for a $FOV = 0.75\,L$ as a function of *SBR*. (*d*) $\overline{\sigma}_{CRB}$ for a $FOV = 0.75\,L$ as a function of N. Other parameters: $N = 500$, $SBR = 5$, unless otherwise stated.

which is attainable with single-photon counting detectors such as avalanche photodiodes. Naturally, the analysis could be extended to represent other detectors by including additional sources of noise. Also, we incorporate the possibility of formally including the prior information needed in these methods to prelocate the molecules. Although we have focused on 2D localization, it is straightforward to generalize the analysis to three dimensions. In the following repositories, https://github.com/lumasullo/sml-ssi and https://github.com/stefani-lab/sml-ssi, we provide a Python open-source code with all functions and scripts used in this work, along with instructions to reproduce all calculations of this study and to vary parameters for other calculations.

The common framework makes it easy to design new approaches. Here, we introduced and characterized two new schemes, OTMIN and RASTMIN. Both schemes achieve the highest localization precision, similar to MINFLUX, and have the potential to be implemented in existing optical systems with minor changes. OTMIN could be implemented in any OT setup by just adding a suitable phase mask to engineer a light focus with an intensity minimum. A similar approach can be used to implement RASTMIN in any laser scanning (confocal) microscope. We believe that these two approaches, RASTMIN in particular, can significantly contribute to a wider application of fluorescence nanoscopy with molecular scale resolution.

We found that all approaches featuring an intensity minimum have a similar performance in the central region of the excitation pattern. Independently of the geometry of the excitation pattern, they outperform methods featuring an intensity maximum by at least a factor of five, reaching, for example, molecular scale precision ($\sim$1 nm) with only $N \sim 1000$ detected photons at an $SBR = 5$.

Because all information is retrieved from the sequence of excitations, SML-SSI does not impose any requirement on the detection geometry. Nonetheless, experimental realizations with confined detection volumes (e.g., confocal detection) could be advantageous to provide higher *SBR* levels. Such implementations and/or varying molecular brightness can be evaluated by varying the *SBR* over the range expected in each case or implementing an ad hoc modification in the provided open-source code.

The results presented consider a perfectly stationary target molecule. Therefore, they provide a maximal attainable localization precision. In practical implementations, the localization precision would be influenced by experimental factors. For example, in single-molecule tracking measurements, the latency of the system as well as the integration time required to obtain the necessary photon counts would become important parameters. For nanoscopic imaging, the setup stability would be critical to achieve the reported theoretical localization precisions.

All of these methods could benefit from iterative and adaptive approaches that update the sequence of excitations with new information about the position of the emitter, as it was done with MINFLUX (11). Methods that use subdiffraction-effective excitation patterns, such as MINSTED or a combination of RASTMAX and STED, can achieve localization precisions as good as methods using minima of light. However, it should be mentioned that in these experiments the total number of detected fluorescence photons N usually corresponds to a much higher number of excitation-emission cycles than in conventional measurements, with the consequent stress on the photostability of the emitter.

Finally, we note that other position estimators might be more suitable than maximum likelihood for different reasons (computational efficiency for real-time calculations, unbiased estimators at low N, etc.). However, we believe that our approach explains thoroughly the fundamental similarities and differences between the different existing methods and will also be a powerful tool to design, develop, and combine new single-molecule localization methods and experiments.

SUPPLEMENTAL MATERIALS

Supplemental materials can be found online at https://doi.org/10.1016/j.bpr.2021.100036.

AUTHOR CONTRIBUTIONS

L.A.M. and F.D.S. conceived the main conceptual ideas of this work. L.A.M. developed the mathematical framework and performed all the calculations and simulations presented in this work. L.F.L. performed calculations and simulations at an early stage of the project. F.D.S. supervised the project. All authors discussed the results and wrote the manuscript.

ACKNOWLEDGMENTS

The authors acknowledge Mariela Sued and Daniela Rodríguez for discussions on the interpretation of some of the results of this work. L.A.M. thanks Iván Lengyel and Felipe Marceca for help with technical aspects of this work and Andrew G. York for inspiring conversations on inverse problems.

F.D.S. acknowledges the support of the Max Planck Society and the Alexander von Humboldt Foundation. This work has been funded by Consejo Nacional de Investigaciones Científicas y Técnicas (CONICET) and Agencia Nacional de Promoción Científica y Tecnológica (ANPCYT), Projects PICT-2017-0870, and PICT-2014-3729.

REFERENCES

1. van Oijen, A. M., P. C. Blainey, …, X. S. Xie. 2003. Single-molecule kinetics of λ exonuclease reveal base dependence and dynamic disorder. *Science.* 301:1235–1238.

2. Yildiz, A., J. N. Forkey, …, P. R. Selvin. 2003. Myosin V walks hand-over-hand: single fluorophore imaging with 1.5-nm localization. *Science.* 300:2061–2065.
3. English, B. P., W. Min, …, X. S. Xie. 2006. Ever-fluctuating single enzyme molecules: Michaelis-Menten equation revisited. *Nat. Chem. Biol.* 2:87–94.
4. Cisse, I. I., I. Izeddin, …, X. Darzacq. 2013. Real-time dynamics of RNA polymerase II clustering in live human cells. *Science.* 341:664–667.
5. Kosuri, P., B. D. Altheimer, …, X. Zhuang. 2019. Rotation tracking of genome-processing enzymes using DNA origami rotors. *Nature.* 572:136–140.
6. van de Linde, S., A. Löschberger, …, M. Sauer. 2011. Direct stochastic optical reconstruction microscopy with standard fluorescent probes. *Nat. Protoc.* 6:991–1009.
7. Lelek, M., M. T. Gyparaki, …, C. Zimmer. 2021. Single-molecule localization microscopy. *Nat. Rev. Methods Prim.* 1:39.
8. Thompson, R. E., D. R. Larson, and W. W. Webb. 2002. Precise nanometer localization analysis for individual fluorescent probes. *Biophys. J.* 82:2775–2783.
9. Mortensen, K. I., L. S. Churchman, …, H. Flyvbjerg. 2010. Optimized localization analysis for single-molecule tracking and super-resolution microscopy. *Nat. Methods.* 7:377–381.
10. Balzarotti, F., Y. Eilers, …, S. W. Hell. 2017. Nanometer resolution imaging and tracking of fluorescent molecules with minimal photon fluxes. *Science.* 355:606–612.
11. Gwosch, K. C., J. K. Pape, …, S. W. Hell. 2020. MINFLUX nanoscopy delivers 3D multicolor nanometer resolution in cells. *Nat. Methods.* 17:217–224.
12. Schmidt, R., T. Weihs, …, S. W. Hell. 2021. MINFLUX nanometer-scale 3D imaging and microsecond-range tracking on a common fluorescence microscope. *Nat. Commun.* 12:1478.
13. Gu, L., Y. Li, …, W. Ji. 2019. Molecular resolution imaging by repetitive optical selective exposure. *Nat. Methods.* 16:1114–1118.
14. Cnossen, J., T. Hinsdale, …, S. Stallinga. 2020. Localization microscopy at doubled precision with patterned illumination. *Nat. Methods.* 17:59–63.
15. Weber, M., M. Leutenegger, …, S. W. Hell. 2021. MINSTED fluorescence localization and nanoscopy. *Nat. Photonics.* 15:361–366.
16. Jouchet, P., C. Cabriel, …, S. Lévêque-Fort. 2021. Nanometric axial localization of single fluorescent molecules with modulated excitation. *Nat. Photonics.* 15:297–304.
17. Reymond, L., T. Huser, …, S. Wieser. 2020. Modulation-enhanced localization microscopy. *J. Phys. Photonics.* 2:041001.
18. Enderlein, J. 2000. Tracking of fluorescent molecules diffusing within membranes. *Appl. Phys. B.* 71:773–777.
19. Levi, V., Q. Ruan, …, E. Gratton. 2003. Scanning FCS, a novel method for three-dimensional particle tracking. *Biochem. Soc. Trans.* 31:997–1000.
20. Berglund, J. J., and H. Mabuchi. 2004. Feedback controller design for tracking a single fluorescent molecule. *Appl. Phys. B.* 78:653–659.
21. Berglund, A., and H. Mabuchi. 2005. Tracking-FCS: fluorescence correlation spectroscopy of individual particles. *Opt. Express.* 13:8069–8082.
22. Ragan, T., H. Huang, …, E. Gratton. 2006. 3D particle tracking on a two-photon microscope. *J. Fluoresc.* 16:325–336.
23. Cohen, A. E., and W. E. Moerner. 2008. Controlling Brownian motion of single protein molecules and single fluorophores in aqueous buffer. *Opt. Express.* 16:6941–6956.
24. Dupont, A., M. Gorelashvili, …, D. Heinrich. 2013. Three-dimensional single-particle tracking in live cells: news from the third dimension. *New J. Phys.* 15:075008.
25. Wehnekamp, F., G. Plucińska, …, D. C. Lamb. 2019. Nanoresolution real-time 3D orbital tracking for studying mitochondrial trafficking in vertebrate axons in vivo. *eLife.* 8:1–22.
26. Davis, L. M., B. K. Canfield, J. P. Wikswo…, 2010. Four-Focus single-particle postion determination in a confocal microscope. *In* Single Molecule Spectroscopy and Imaging III. J. Enderlein, K. G. Zygmunt, and E. Rainer, eds. SPIE, pp. 140–149.
27. Germann, J. A., and L. M. Davis. 2014. Three-dimensional tracking of a single fluorescent nanoparticle using four-focus excitation in a confocal microscope. *Opt. Express.* 22:5641–5650.
28. Perillo, E. P., Y. L. Liu, …, A. K. Dunn. 2015. Deep and high-resolution three-dimensional tracking of single particles using nonlinear and multiplexed illumination. *Nat. Commun.* 6:7874.
29. Zhang, C., and K. Welsher. 2021. Information-efficient, off-center sampling results in improved precision in 3D single-particle tracking microscopy. *Entropy (Basel).* 23:498.
30. Hellriegel, C., and E. Gratton. 2009. Real-time multi-parameter spectroscopy and localization in three-dimensional single-particle tracking. *J. R. Soc. Interface.* 6 (*Suppl 1*):S3–S14.
31. Kis-Petikova, K., and E. Gratton. 2004. Distance measurement by circular scanning of the excitation beam in the two-photon microscope. *Microsc. Res. Tech.* 63:34–49.
32. Marklund, E., B. van Oosten, …, S. Deindl. 2020. DNA surface exploration and operator bypassing during target search. *Nature.* 583:858–861.
33. Hell, S. W., and J. Wichmann. 1994. Breaking the diffraction resolution limit by stimulated emission: stimulated-emission-depletion fluorescence microscopy. *Opt. Lett.* 19:780–782.
34. Klar, T. A., S. Jakobs, …, S. W. Hell. 2000. Fluorescence microscopy with diffraction resolution barrier broken by stimulated emission. *Proc. Natl. Acad. Sci. USA.* 97:8206–8210.
35. Wang, Q., and W. E. Moerner. 2010. Optimal strategy for trapping single fluorescent molecules in solution using the ABEL trap. *Appl. Phys. B.* 99:23–30.
36. Thiele, J. C., D. A. Helmerich, …, J. Enderlein. 2020. Confocal fluorescence-lifetime single-molecule localization microscopy. *ACS Nano.* 14:14190–14200.
37. Masullo, L. A., F. Steiner, …, F. D. Stefani. 2021. Pulsed interleaved MINFLUX. *Nano Lett.* 21:840–846.
38. Kay, S. M. 1995. Fundamentals of Statistical Signal Processing: Estimation Theory. Prentice Hall PTR, Upper Saddle River, New Jersey.
39. Ober, R. J., S. Ram, and E. S. Ward. 2004. Localization accuracy in single-molecule microscopy. *Biophys. J.* 86:1185–1200.
40. Abraham, A. V., S. Ram, …, R. J. Ober. 2009. Quantitative study of single molecule location estimation techniques. *Opt. Express.* 17:23352–23373.
41. Chao, J., E. Sally Ward, and R. J. Ober. 2016. Fisher information theory for parameter estimation in single molecule microscopy: tutorial. *J. Opt. Soc. Am. A Opt. Image Sci. Vis.* 33:B36–B57.
42. Gill, R. D., and B. Y. Levit. 1995. Applications of the van Trees inequality: a Bayesian Cramér-Rao bound. *Bernoulli.* 1:59–79.
43. van Trees, H. L. 1968. Detection, Estimation, and Modulation Theory. Part I: Detection, Estimation, and Linear Modulation Theory. John Wiley & Sons, New York.
44. Kasper, R., B. Harke, …, M. Sauer. 2010. Single-molecule STED microscopy with photostable organic fluorophores. *Small.* 6:1379–1384.
45. Szalai, A. M., B. Siarry, …, F. D. Stefani. 2021. Super-resolution imaging of energy transfer by intensity-based STED-FRET. *Nano Lett.* 21:2296–2303.
46. Masullo, L. A., A. M. Szalai, L. F. Lopez, and F. D. Stefani. 2021. Fluorescence nanoscopy at the sub-10 nm scale. *Biophysical Reviews* https://doi.org/10.1007/s12551-021-00864-z.